RSC Advances

PAPER

View Article Online
View Journal | View Issue

Open Access Article. Published on 14 April 2023. Downloaded on 3/13/2026 7:11:50 AM.
This article is licensed under a Creative Commons Attribution-NonCommercial 3.0 Unported Licence.

Check for updates

Cite this: *RSC Adv.*, 2023, **13**, 11742

Two-dimensional $Pd_3(AsSe_4)_2$ as a photocatalyst for the solar-driven oxygen evolution reaction: a first-principles study†

Zhen Gao,[a] Xin He,[a] Wenzhong Li,[a] Yao He *[a] and Kai Xiong[b]

Received 28th January 2023
Accepted 17th March 2023

DOI: 10.1039/d3ra00592e

rsc.li/rsc-advances

The relationship between the structure and properties of materials is the core of material research. Bulk $Pd_3(PS_4)_2$ materials have been successfully synthesized in the field of three-dimensional materials. After that, various studies on two-dimensional layered materials were conducted. Inspired by these successes, this work used density functional theory based on first principles to explore similar two-dimensional $Pd_3(AsX_4)_2$, where X is S, Se, or Te belonging to the same group. Our findings demonstrate that the $Pd_3(AsS_4)_2$ and $Pd_3(AsSe_4)_2$ monolayers, with HSE06 band gaps of 2.37 and 1.36 eV, respectively, are indirect semiconductors. Additionally, their carrier mobilities [523.23 $cm^2\ s^{-1}\ V^{-1}$ and 440.6 $cm^2\ s^{-1}\ V^{-1}$] are also proved to be superior to MoS_2 [~200 $cm^2\ s^{-1}\ V^{-1}$]. The optical calculations indicate that the $Pd_3(AsSe_4)_2$ monolayer yields suitable valence band edge positions for the visible-light-driven water splitting reactions. More interestingly, at a low applied voltage of 0.14 V, $Pd_3(AsSe_4)_2$ exhibits outstanding oxygen evolution reaction performance. In this study, the possible mechanism for the ability of $Pd_3(AsSe_4)_2$ monolayer to promote photocatalysis and oxygen evolution was explained, which may pave the way for the practical design of further solar-driven high-quality water splitting photocatalysis.

Introduction

To address the environmental issues brought by the combustion of fossil fuels that significantly alleviated the energy crisis, research on renewable clean energy, such as solar energy, has sparked a boom in the field of materials science and chemistry.[1,2] Therefore, the search for two-dimensional (2D) materials that can serve as highly effective photovoltaic (PV) solar cells and water splitting catalysts present an attractive prospect for providing clean and sustainable energy without burning fossil fuels or releasing chemical pollutants.[3–6] Many materials have been identified as having photocatalytic potential[7–11] since the first TiO_2 photocatalytic water splitting demonstration by Fujishima and Honda in 1972.[12] Two half-reactions, the oxygen evolution reaction (OER) and hydrogen evolution reaction (HER), where OER is a four-electron process and HER is a two-electron process, make up the entire process of photocatalytic water splitting. As a result, OER is more complicated than HER and is typically regarded as the step reaction process that determines the rate throughout the entire water splitting process.[13,14] Research on 2D materials has entered a period of rapid development ever since Novoselov and Geim successfully synthesized monolayer graphene in 2004, which showed exceptional physical properties, such as enormous specific surface area and high carrier mobility.[15] These characteristics also make 2D materials suitable for a variety of electronic,[16–19] optoelectronic,[20–23] and plasma devices.[24–26]

For photocatalytic water decomposition and oxygen evolution, 2D materials, such as g-C_3N_4 (0.43 V),[27] β-GeSe (0.497 V),[9] and $TlPt_2S_3$ (2.46 V),[11] have been reported to be excellent catalysts. However, the disadvantage is that these materials require a considerable amount of additional voltage. Therefore, in order to solve the issue of increasing energy demand in the future, it is crucial to investigate 2D semiconductor materials with proper band gaps and low reaction voltages for oxygen evolution.

Palladium thiophosphate ($Pd_3(PS_4)_2$), the layered crystal, was initially synthesized in 1971 by Bither *et al.*[28] Later, through theoretical investigations, Jing and Tang *et al.* discovered that 2D layered $Pd_3(PS_4)_2$ has excellent photocatalytic water splitting capabilities.[29–32] Given that both P and As atoms are in group-VA of the periodic table, while S, Se, and Te atoms are in group-VIA, substituting atoms of the same group in similar configurations may result in similar or even better properties. Inspired by this, in this study, we investigated the dynamical stability, mechanical, electronic, and photocatalytic water splitting properties of $Pd_3(AsX_4)_2$ (X = S, Se, and Te) monolayers using the density functional theory (DFT) calculations.

[a]*Department of Physics, Yunnan University, Kunming 650091, People's Republic of China. E-mail: yhe@ynu.edu.cn*

[b]*Materials Genome Institute, School of Materials and Energy, Yunnan University, Kunming 650091, P. R. China*

† Electronic supplementary information (ESI) available. See DOI: https://doi.org/10.1039/d3ra00592e

© 2023 The Author(s). Published by the Royal Society of Chemistry

Open Access Article. Published on 14 April 2023. Downloaded on 3/13/2026 7:11:50 AM. This article is licensed under a Creative Commons Attribution-NonCommercial 3.0 Unported Licence.

Computational details

Our DFT computations were performed using the Vienna ab initio simulation package (VASP),[33] and the projector augmented wave (PAW)[34] method was utilized to describe the ion–electron interactions. The Perdew–Burke–Ernzerhof functional (PBE)[35] within the generalized gradient approximation (GGA) was used throughout our computations. A hybrid functional based on the Heyd–Scuseria–Ernzerhof (HSE06) exchange–correlation functional[36] was adopted for accurately calculating the band structure and absorption properties. The energy cut-off of the plane waves was set to 400 eV. The structures were fully relaxed until the maximum force on each atom was less than 0.005 eV Å^{-1}, and the energy convergence criterion in the self-consistent calculations was set to 10^{-5} eV. The 4 × 4 × 1 and 8 × 8 × 1 Monkhorst–Pack *k*-point grids were used for geometry optimizations and self-consistent calculations, respectively. A vacuum region of at least 20 Å in the *z* direction was adopted to avoid artificial interactions between the neighboring layers. The phonon dispersion was calculated using the Phonopy code[37] within the density functional perturbation theory (DFPT).[38] In phonon calculations, a supercell is used with 2 × 2 × 1 and an atomic displacement distance of 0.01 Å. A finer *k*-point grid of 2π × 0.02 Å^{-1} was employed. To further confirm the thermal stability of the 2D $Pd_3(AsX_4)_2$ (X = S, Se, and Te) monolayers, the *ab initio* molecular dynamics (AIMD) simulation within the canonical ensemble (NVT) and Nosé–Hoover thermostat at 300 K and 500 K were carried out on a 3 × 3 × 1 supercell. At each temperature, the AIMD simulation in the NVT ensemble lasted for 5 ps with a time step of 1.0 fs.

For the investigation of optical properties, according to the following expression, the light absorption coefficients of the structures are calculated:[39]

$$\alpha(\omega) = \sqrt{2}\,\frac{\omega}{c}\left[\sqrt{\varepsilon_1{}^2(\omega) + \varepsilon_2{}^2(\omega)} - \varepsilon_1(\omega)\right]^{\frac{1}{2}}$$

Thus, in the dielectric equation, ε_1 and ε_2 stand for the real and imaginary parts, respectively. In this, the contribution of interband transition is used to calculate ε_2:[40]

$$\varepsilon_2(\omega) = \frac{4\pi^2 e^2}{\Omega}\lim_{q\to 0}\frac{1}{q^2}\sum_{c,v,k} 2\omega_k \delta\left(\varepsilon_{ck} - \varepsilon_{vk} - \omega\right) \times \left\langle u_{ck+e_\alpha q}\middle| u_{vk}\right\rangle \times \left\langle u_{ck+e_\beta q}\middle| u_{vk}\right\rangle^*$$

where Ω expresses the unit cell volume. q is the Bloch vector of the incident wave. w_k is the k-point weight. c and v represent the conduction band state and the valence band state, respectively. u_{ck} represents the cell periodic part of the orbitals at point k. Kramers–Kronig transformation was used to determine the real part ε_1:[40]

$$\varepsilon_1(\omega) = 1 + \frac{2}{\pi} P \int_0^\infty \frac{\omega' \varepsilon_2(\omega)}{(\omega')^2 - \omega^2 + \mathrm{i}\eta}\mathrm{d}\omega'$$

where P is the principle value. η denotes the complex shift in the Kramers–Kronig transformation.

We simulated the OER reaction under the neutral condition of pH = 7 and temperature for 300 K in order to quantify the performance of the OER and understand the underlying photocatalytic mechanism. The expressions below illustrate how this procedure can be broken down into four phases:[41]

$$* + H_2O \rightarrow *OH + H^+ + e^-$$

$$*OH \rightarrow *O + H^+ + e^-$$

$$*O + H_2O \rightarrow *OOH + H^+ + e^-$$

$$*OOH \rightarrow * + O_2 + H^+ + e^-$$

where * denotes a free position on the surface that can be adsorbed, and *OH, *O, and *OOH denote the OH, O, and OOH intermediates adsorbed on the surface, respectively.

We used a method established by Nørskov *et al.*[42] to calculate the free energy change (ΔG) in the water oxidation reactions. This method states that the ΔG of an electrochemical reaction is computed as

$$\Delta G = \Delta E + \Delta E_{ZPE} - T\Delta S + \Delta G_U + \Delta G_{pH}$$

where ΔE is the adsorption energy, $\Delta E_{ZPE,}$ and ΔS are the differences in zero point energy and entropy difference between the adsorbed state and the gas phase, respectively. We used a finite difference method to calculate the vibration frequencies of all adsorbed species for entropy and zero-point energy.[43] T stands for the ambient temperature (300 K). The free energy contributed in different pH concentrations is represented by ΔG_{pH} ($\Delta G_{pH} = k_B T \times \ln 10 \times$ pH). ΔG_U ($\Delta G_U = -eU$) signifies extra potential bias produced by an electron in the electrode, where U represents the electrode potential with respect to the standard hydrogen electrode (SHE).

Results and discussion

Structures and stabilities

We first explored 2D $Pd_3(AsX_4)_2$ compounds with lattice structures similar to that of $Pd_3(PS_4)_2$. For X covering the group-VIA elements (S, Se, and Te). Fig. 1 depicts the monolayer $Pd_3(AsX_4)_2$ (X = S, Se, and Te) crystal structure. The optimized lattice parameters are $a = b = 6.882$ (7.180 and 7.569) Å for the $Pd_3(AsX_4)_2$ (X = S, Se, and Te) monolayers, which crystallize in the $P\bar{3}m1$ space group. Due to the varying radii of various atoms, the lattice constants of the $Pd_3(AsX_4)_2$ (X = S, Se, Te) monolayers are slightly larger than that of the $Pd_3(PS_4)_2$ ($a = b = 6.64$ Å) monolayer.[30] The detailed structural information of the three layers is listed in Table 1. We calculated the electron localization function (ELF) to describe the bonding behavior in the structure. As shown in Fig. 1b, electrons are primarily localized between As–X (X = S, Se, and Te) atoms. In contrast, there are no electron localizations between the X–Pd (X = S, Se, and Te) atoms. The above results reflect the covalent bonding states between the As and X (X = S, Se, and Te) atoms and the ionic bonding between X (X = S, Se, and Te) and Pd atoms.

To assess the thermodynamic stabilities of the $Pd_3(AsX_4)_2$ (X = S, Se, Te) monolayers, we first calculated their cohesive energy using the following equation:

Open Access Article. Published on 14 April 2023. Downloaded on 3/13/2026 7:11:50 AM.
This article is licensed under a Creative Commons Attribution-NonCommercial 3.0 Unported Licence.

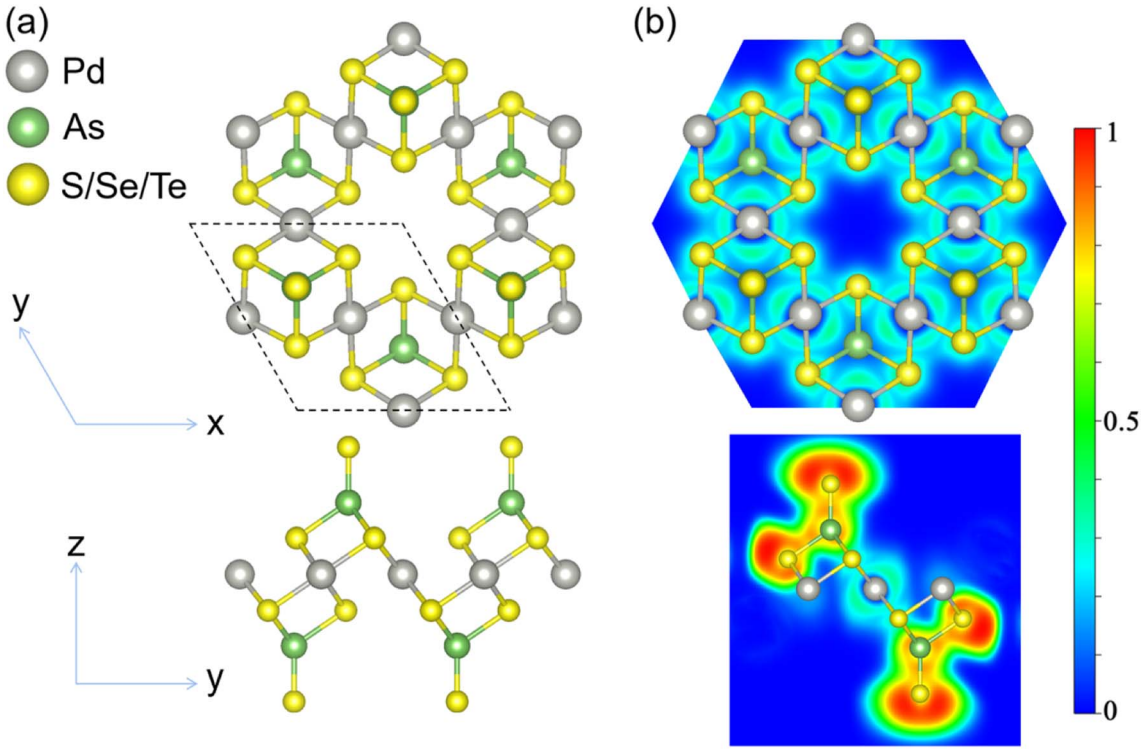

Fig. 1 (a) Atomic structure of the $Pd_3(AsX_4)_2$ (X = S, Se, and Te) monolayer. The dashed line represents the primitive cell. (b) The electron localization function (ELF). The isosurface for ELF is 0.75e $Å^{-3}$.

Table 1 Lattice parameter L_p (in Å), space group, cohesive energy E_{coh} (in eV per atom), and formation energy ΔH_f (in eV per atom) for monolayers $Pd_3(AsX_4)_2$ (X = S, Se, Te)

Phase	L_p	Space group	E_{coh}	ΔH_f
$Pd_3(AsS_4)_2$	$a = b = 6.882$	$P\bar{3}m1$	−4.28	−4.18
$Pd_3(AsSe_4)_2$	$a = b = 7.180$	$P\bar{3}m1$	−3.74	−3.18
$Pd_3(AsTe_4)_2$	$a = b = 7.569$	$P\bar{3}m1$	−3.56	−3.53

$$E_{coh} = [E(Pd_xAs_yX_z) - xE(Pd) - yE(As) - zE(X)]/(x + y + z)$$

where x, y, and z represent the number of atoms in the cell, $E(Pd_xAs_yX_z)$ is the total energy of the $Pd_3(AsX_4)_2$ (X = S, Se, and Te) layers, E(Pd), E(As), and E(X) are the energies of the isolated Pd, As, and X atoms, respectively. A more negative E_{coh} value, by this definition, denotes higher thermodynamic stability. $Pd_3(AsS_4)_2$, $Pd_3(AsSe_4)_2$, and $Pd_3(AsTe_4)_2$ monolayers have computed cohesive energies of −4.28, −3.89, and −3.56 eV per atom, respectively, which are lower than those of Cu_2Si (−3.46 eV per atom),[44] silicene (−3.98 eV per atom),[44] and germanene (−3.26 eV per atom)[44] monolayers at the same theoretical level, and the cohesive energy of $Pd_3(AsS_4)_2$ is equivalent to that of the $Pd_3(PS_4)_2$ (−4.55 eV per atom) monolayer. The relatively small cohesive energies of 2D $Pd_3(AsX_4)_2$ compounds suggest that the monolayers are stable phases of Pd–X–As systems. We should note, especially for the compound, which has not yet been synthesized, the negative values of the cohesive and formation energies are necessary. Next, we calculated the formation energy of the $Pd_3(AsX_4)_2$ monolayers. The formation energy (ΔH_f) is defined as the difference between the energy of a crystal and corresponding constituent elements in their standard states. The formation energy is given by the following expression:

$$\Delta H_f = [E(Pd_xAs_yX_z) - x\mu(Pd) - y\mu(As) - z\mu(X)]/(x + y + z)$$

where x, y, and z represent the number of atoms in the cell, $E(Pd_xAs_yX_z)$ is the total energy of the $Pd_3(AsX_4)_2$ (X = S, Se, and Te) layers. μ(Pd), μ(As), and μ(X) are the chemical potentials of Pd, As, and X (X = S, Se, and Te), respectively. For most elements, chemical potentials are equal to the DFT total energies of their ground states.[45] Table 1 provides the obtained values of ΔH_f. The negative values of the formation energies of $Pd_3(AsX_4)_2$ (X = S, Se, and Te) monolayers indicate the stability of these compounds. For a material to be thermodynamically stable, it is necessary but not sufficient that $\Delta H_f < 0$. Indeed, thermodynamic stability requires that ΔH_f be negative not only relative to its pure elemental phases but relative to all other competing phases, *i.e.*, its energy must be below the convex hull.[46] Thus, we calculated the energy above the convex hull (ΔH_{hull}) by using the following formula,

$$\Delta H_{hull} = \Delta H_f - \Delta H$$

where ΔH_f is the formation energy of the $Pd_3(AsX_4)_2$ (X = S, Se, and Te) monolayers, ΔH is the convex hull energy at the $Pd_3(AsX_4)_2$ (X = S, Se, and Te) composition. When $\Delta H_{hull} < 0$, it

 © 2023 The Author(s). Published by the Royal Society of Chemistry

Open Access Article. Published on 14 April 2023. Downloaded on 3/13/2026 7:11:50 AM. This article is licensed under a Creative Commons Attribution-NonCommercial 3.0 Unported Licence.

indicates that the structure is thermodynamically stable. By calculation, we found that the ΔH_{hull} of the $Pd_3(AsS_4)_2$ structure is 0.02 eV per atom. Due to the DFT-related uncertainty/calculation error problem, ΔH_{hull} can be considered thermodynamically stable at less than 0.025 eV per atom.[45] Therefore, it is thermodynamically stable for the $Pd_3(AsS_4)_2$ monolayer. Similarly, we calculated the two structures $Pd_3(AsSe_4)_2$ and $Pd_3(AsTe_4)_2$ and found that the ΔH_{hull} for the $Pd_3(AsSe_4)_2$ structure is 0.03 eV per atom, which is very close to 0.025 eV per atom. Therefore, the $Pd_3(AsSe_4)_2$ structure is also considered to be thermodynamically stable. However, the $Pd_3(AsTe_4)_2$ structure has energy above the convex hull of as high as 0.3 eV per atom, indicating that it is thermodynamically unstable. So, the $Pd_3(AsTe_4)_2$ structure is not sufficient to establish its experimental growth. Therefore, we further explored the other stability of the $Pd_3(AsX_4)_2$ (X = S, Se, and Te) structure.

Based on the elastic stability criteria,[47] stable 2D $Pd_3(AsX_4)_2$ (X = S, Se, and Te) lattices should satisfy C_{11}, C_{22}, $C_{66} > 0$ and $C_{11}C_{22} > C_{12}^2$, where C_{ij} are the elastic constants. The summarized values shown in Table S1† indicate that the criteria are fully satisfied. Then, as shown in Fig. 2a–c, we calculated the phonon dispersion along the high-symmetry lines in the first Brillouin zone to assess the dynamical stabilities of $Pd_3(AsX_4)_2$ (X = S, Se, and Te) monolayers. There is not any appreciable imaginary frequency in the phonon spectrum of these $Pd_3(AsX_4)_2$ (X = S, Se, and Te) monolayers, suggesting the dynamical stabilities of these different structures.

We further performed AIMD simulations to evaluate the thermal stabilities of $Pd_3(AsX_4)_2$ (X = S, Se, and Te) monolayers. We used a relatively large 3 × 3 supercell and carried out AIMD simulations at the temperatures of 300 K and 500 K for $Pd_3(AsX_4)_2$ (X = S, Se, and Te) monolayers. The energy of monolayers $Pd_3(AsX_4)_2$ (X = S and Se) changes only in a small range (~0.1 eV per atom), as shown in Fig. S1 of the ESI,† and its structure can be successfully preserved through the simulation time. For the $Pd_3(AsTe_4)_2$ monolayer, however, the structure collapses after the simulation, making it unstable at ambient temperature, which is consistent with the results of ΔH_{hull}. Thus, in the following discussion, we will mainly focus on $Pd_3(AsS_4)_2$ and $Pd_3(AsSe_4)_2$ monolayers. After that, we performed AIMD simulations of the $Pd_3(AsS_4)_2$ and $Pd_3(AsSe_4)_2$ monolayers at 500 K, as shown in Fig. S2 of the ESI.† At the end of the simulations, we found that both the structures could still be maintained and the energy fluctuated in a small range, as shown in Fig. S2 of the ESI.† Meanwhile, we investigated the chemical stability of $Pd_3(AsS_4)_2$ and $Pd_3(AsSe_4)_2$ monolayers, which is the capacity of 2D materials to preserve their original physical and chemical properties in the environment. We used the surface work function to evaluate the chemical stability of the monolayers $Pd_3(AsS_4)_2$ and $Pd_3(AsSe_4)_2$.[48] Their physical meaning is described as the essential energy to remove an electron from the Fermi level. A low work function means that the electrons are loosely bound, which is advantageous for carrier transfer during the photocatalytic process but detrimental to the chemical stability of the material.[9] Here, we merely take into account the work function of the vacuum environment monolayers of $Pd_3(AsS_4)_2$ and $Pd_3(AsSe_4)_2$. The monolayers $Pd_3(AsS_4)_2$ and $Pd_3(AsSe_4)_2$ (5.5 and 5.43 eV) have greater work functions than black phosphorene (4.50 eV),[49] as illustrated in Fig. S3,† demonstrating their exceptional chemical stability. The $Pd_3(AsS_4)_2$ and $Pd_3(AsSe_4)_2$ monolayers are energetically, dynamically, thermally, and chemically stable, according to these systematic studies.

Electronic and transport properties

We will now look into their electronic properties. Based on band structure calculations using the PBE method, it was found that the $Pd_3(AsS_4)_2$ and $Pd_3(AsSe_4)_2$ monolayers are direct and indirect semiconductors with a band gap of 1.37 eV and 0.68 eV, respectively. The valence band maximum (VBM) and conduction band minimum (CBM)of the $Pd_3(AsS_4)_2$ monolayer are both located at the Γ point. However, for the $Pd_3(AsSe_4)_2$ monolayer, the VBM is at the M point, while CBM is at the Γ point, as illustrated in Fig. 3a and c. The projected density of states (PDOS) on the atomic orbitals is also shown in Fig. 4a and b. It is evident that the d orbital of Pd and p orbital of S (Se) both make a major contribution to the Fermi energy and exhibit a certain orbital hybridization effect. The electronic states of CBM and VBM in $Pd_3(AsS_4)_2$ and $Pd_3(AsSe_4)_2$ monolayers are also studied in order to better investigate the charge distribution of $Pd_3(AsS_4)_2$ and $Pd_3(AsSe_4)_2$ monolayers. For the $Pd_3(AsS_4)_2$ monolayer, as shown in Fig. 4c and d, VBM demonstrates that electrons are localized around all Pd atoms and some S atoms, while CBM comes from all S atoms and some Pd atoms. In contrast to the $Pd_3(AsS_4)_2$ monolayer, the VBM of the $Pd_3(AsSe_4)_2$ monolayer exhibits a concentration of all electrons around Pd atoms, whereas the CBM contains both Pd atoms and Se atoms. These findings are in line with the results of the PDOS results on $Pd_3(AsS_4)_2$ and $Pd_3(AsSe_4)_2$ monolayers.

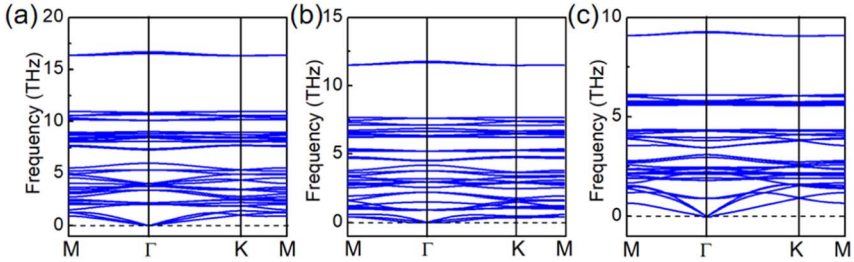

Fig. 2 (a–c) Phonon dispersions of $Pd_3(AsS_4)_2$, $Pd_3(AsSe_4)_2$ and $Pd_3(AsTe_4)_2$ monolayers, respectively.

Open Access Article. Published on 14 April 2023. Downloaded on 3/13/2026 7:11:50 AM.
This article is licensed under a Creative Commons Attribution-NonCommercial 3.0 Unported Licence.

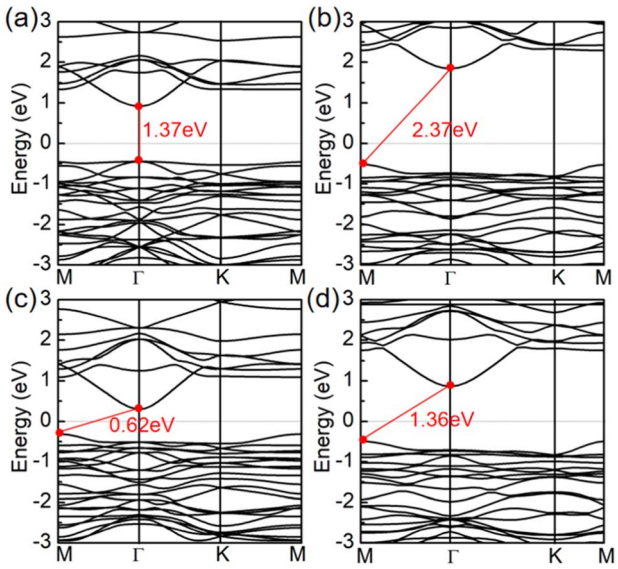

Fig. 3 Band structures of $Pd_3(AsS_4)_2$ and $Pd_3(AsSe_4)_2$ monolayers by the (a and c) PBE and (b and d) HSE06 methods.

It is well-known that the PBE functional generally underestimates the band gap by about 30%;[50] we thus carried out the hybrid density functional (HSE06) calculations to achieve a more accurate band gap. The band gaps of $Pd_3(AsS_4)_2$ and $Pd_3(AsSe_4)_2$ monolayers are 2.37 eV (Fig. 3b) and 1.36 eV (Fig. 3d), respectively, according to the HSE06 calculations. The direct band gap of the $Pd_3(AsS_4)_2$ monolayer becomes an indirect band gap at this time. At the same time, we also analyzed the PDOS by using the HSE06 method, as shown in Fig. S4.† We found that the HSE06 results are generally consistent with the PBE results. The activity and water-splitting efficiency of a photocatalyst are greatly influenced by the band gap and the electronic band structure. As previously reported, the band gap should be between 1.23 eV and 3.00 eV, in order to realize an efficient light-harvesting photocatalyst for water splitting.[51] $Pd_3(AsX_4)_2$ (X = S and Se) monolayers perfectly satisfy this criterion because they have band gap values of 2.37 and 1.36 eV, respectively.

The efficiency of photocatalysis will decline if the rate of electrons and hole recombination is high. Two-dimensional materials, which have a low dimension and a high rate of carrier migration compared to three-dimensional ones, are better equipped to prevent the compounding of photo electron–hole pairs. An increase in carrier mobility leads to higher photocatalytic efficiency as it allows for faster transport to the photocatalyst surface. Moreover, it is preferable to suppress the recombination of electrons and holes, which can be achieved by the difference between electron and hole mobilities in the same direction.[52]

Therefore, to illustrate the carrier mobilities along the x and y directions, rectangular lattices (Fig. S5†) were used. The effective masses of carriers, which depend on the band structure of the region around the band edges, were determined by fitting a linear function to the CBM (electrons) and VBM (holes) using the following equation:

$$m^* = \frac{1}{\hbar^2}\frac{\partial^2 E(k)}{\partial k^2}$$

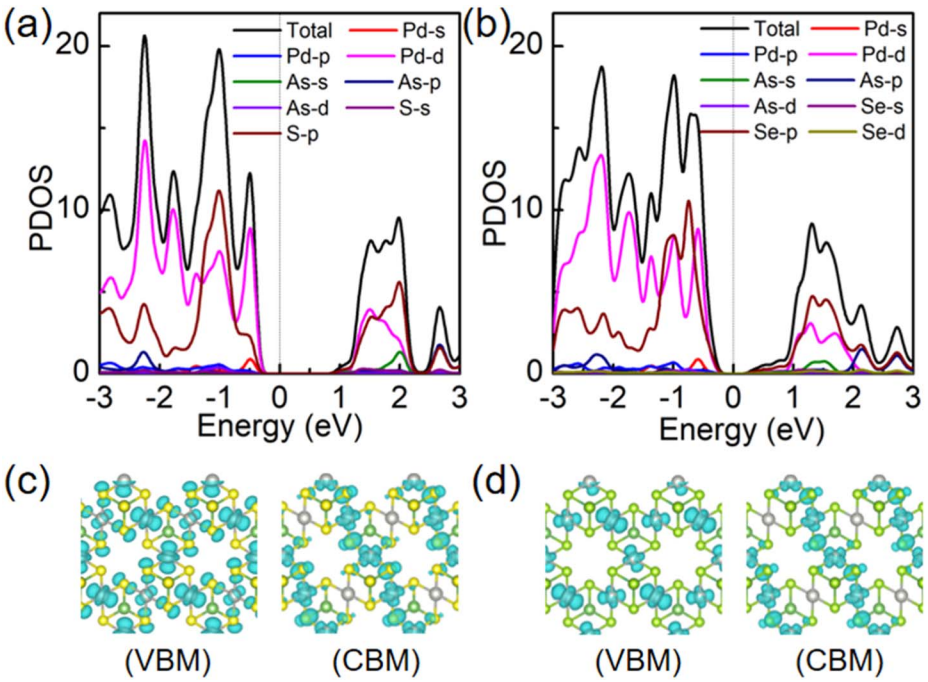

Fig. 4 Projected density of states (PDOS) of (a) $Pd_3(AsS_4)_2$ and (b) $Pd_3(AsSe_4)_2$ monolayers by the PBE method. Partial charge density distributions of the VBM and CBM for (c) $Pd_3(AsS_4)_2$ and (d) $Pd_3(AsSe_4)_2$ monolayers by the PBE method. The isosurface is set to be 0.006e Å^{-3}.

 © 2023 The Author(s). Published by the Royal Society of Chemistry

Open Access Article. Published on 14 April 2023. Downloaded on 3/13/2026 7:11:50 AM. This article is licensed under a Creative Commons Attribution-NonCommercial 3.0 Unported Licence.

where $E(k)$ represents the energy at the band boundaries as a function of wave number k. Table 2 displays the results obtained for the carrier effective mass m^*.

The in-plane stiffness (C_{2D}) can be calculated by simulating the total energy (E) change of the applied strain (ε) motivated by the 2D materials with the equation $C_{2D} = [\partial^2 E/\partial\varepsilon^2]/S_0$, where S_0 is the surface area of the optimized supercell. The linear relationship between the band edge for VBM and CBM and the strain exertion (ε) along the x and y direction, respectively, was fitted to estimate the Deformation Potentials (DP) constant (E_1).

According to the DP theory, the following expression can be used to determine the carrier mobility of 2D materials,[53]

$$\mu_{2D} = \frac{2e\hbar^3 C_{2D}}{3k_B T|m^*|^2 E_1{}^2}$$

Here, $\hbar$ is the reduced Planck constant, k_B is the Boltzmann constant, and T is the temperature (set to be 300 K). The carrier mobilities of $Pd_3(AsS_4)_2$ and $Pd_3(AsSe_4)_2$ monolayers along different directions can be calculated by a straightforward application of the expression above because C_{2D}, m^* as well as E_1 have already been estimated. The calculated carrier mobilities are listed in Table 2. The electron carrier mobility of $Pd_3(AsS_4)_2$ and $Pd_3(AsSe_4)_2$ are 523.23 $cm^2\ s^{-1}\ V^{-1}$ and 440.6 $cm^2\ s^{-1}\ V^{-1}$, respectively, which are significantly higher than those of MoS_2 [~200 $cm^2\ s^{-1}\ V^{-1}$][54] and GeP_3 [~190 $cm^2\ s^{-1}\ V^{-1}$].[55] The hole carrier mobility of $Pd_3(AsS_4)_2$ and $Pd_3(AsSe_4)_2$ are 0.198 and 12.72 $cm^2\ s^{-1}\ V^{-1}$, respectively, indicating that they are both electron-transport semiconductors. Such high electron carrier mobilities make it possible for carriers to migrate rapidly to the surface. The large difference of electron and hole mobilities in the same direction can effectively suppress the recombination of the photo-generated electron–hole pairs, thus effectively improving the photocatalytic performance of $Pd_3(AsS_4)_2$ and $Pd_3(AsSe_4)_2$.

Strain effect on the electronic property

Previous studies have shown that external strain can have a significant impact on the electronic and optical properties of materials.[56,57] In actuality, the substrates that are employed to support the 2D materials make strain effects inescapable. We found that these 2D materials have excellent mechanical properties, as shown in Fig. S6.† The strain–stress diagram S6† shows that the $Pd_3(AsS_4)_2$ and $Pd_3(AsSe_4)_2$ monolayers can maintain the ideal strain of 48% and 50%, respectively, which is much larger than that of other well-known 2D materials such as molybdenum disulfide (20%)[58] and graphene (24%),[59] indicating the high mechanical strength and excellent mechanical properties of the $Pd_3(AsS_4)_2$ and $Pd_3(AsSe_4)_2$ monolayers. New insights into the applications of flexible electrical and photonic devices will be revealed by the modulation of the band gap and electronic structure by strain. Using the PBE functional, the band gap as a function of the biaxial strain is plotted in Fig. 5. Based on the different band structures, two strain zones can be distinguished with clarity. For the $Pd_3(AsS_4)_2$ monolayer, zone I is for an indirect band gap with a strain range of 2–10%, where the band gap initially increases and reaches its maximal value of 1.79 eV at 8% strain before rapidly decreasing with further expansion. It should be noted that increasing the strain up to 10% (gap, 1.75 eV) will not cause the gap to disappear completely. Nevertheless, 2D $Pd_3(AsS_4)_2$ transforms into a direct band gap semiconductor in the strain range of −5 to 2% (zone II). The direct band gap, however, transforms into an indirect band gap when the strain hits −5%, and when the compressive strain reaches 10%, the band gap still does not go away completely. As a result, the $Pd_3(AsS_4)_2$ monolayer exhibits semiconductor characteristics in the strain range of −10 to 10% (Fig. 5a). For the $Pd_3(AsSe_4)_2$ monolayer, zone I corresponds to an indirect band gap with the strain ranging from −7 to 10%, where the band gap is gradually increased. It should be observed that increasing the strain up to 10% (gap, 1.18 eV) is not able to make the gap disappear, and stretching the material results in no band gap transition. Most interestingly, zone III demonstrates that the $Pd_3(AsSe_4)_2$ monolayer's band gap decreases to zero when the compressive strain exceeds −7% and the material transforms into a metal (Fig. 5b). Fig. S7† illustrates that the semiconductor-to-metal transition is caused by the downward shift of the CBM and an upward movement of VBM, for the monolayer $Pd_3(AsSe_4)_2$. The change in band gap suggests that the semiconductor can be tailored for specific electronic applications.

Photocatalytic properties

To evaluate the potential of the material for photocatalysis, it is necessary to investigate its optical characteristics and determine whether it meets the required band gap.

In the visible light region (350–700 nm),[60] we found that only the $Pd_3(AsSe_4)_2$ structure exhibits high absorption efficiency, while the absorption efficiency of the $Pd_3(AsS_4)_2$ structure is poor, indicating that $Pd_3(AsSe_4)_2$ has a greater potential for photocatalytic applications (Fig. 6a).

The energy levels of the VBM and CBM must, respectively, be lower and greater than the water oxidation and reduction

Table 2 Calculated effective mass $|m^*|$, DP constant $|E_1|$, in-plane stiffness C_{2D} (in N m^{-1}), carrier mobility μ ($cm^2\ s^{-1}\ V^{-1}$) for $Pd_3(AsS_4)_2$ and $Pd_3(AsSe_4)_2$ monolayers along the x and y directions

Phase	Carrier type	$\lvert m_x^*\rvert/m_0$	$\lvert m_y^*\rvert/m_0$	$\lvert E_{1x}\rvert$	$\lvert E_{1y}\rvert$	C_{2Dx}	C_{2Dy}	μ_x	μ_y
$Pd_3(AsS_4)_2$	Hole	9.32	12.97	3.43	3.44	14.5	13.0	0.198	0.092
	Electron	1.05	1.00	0.59	0.81			523.23	280.75
$Pd_3(AsSe_4)_2$	Hole	1.15	1.60	2.31	3.32	10.3	9.9	2.166	12.72
	Electron	1.64	1.36	0.56	0.41			168.55	440.6

Open Access Article. Published on 14 April 2023. Downloaded on 3/13/2026 7:11:50 AM.
This article is licensed under a Creative Commons Attribution-NonCommercial 3.0 Unported Licence.

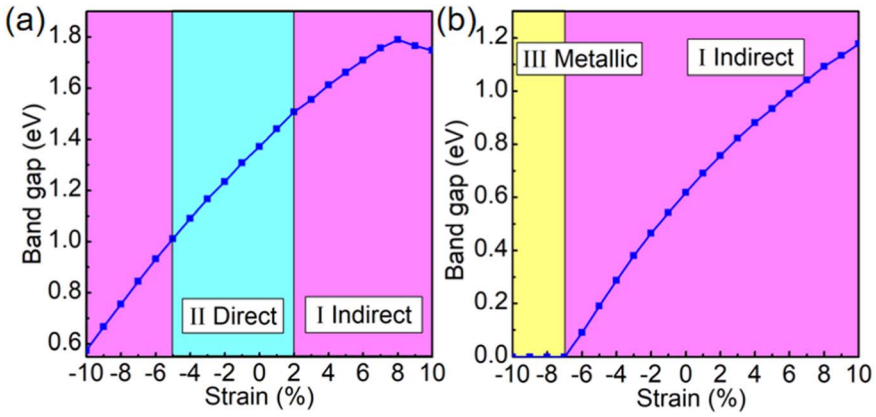

Fig. 5 Band gaps of the (a) $Pd_3(AsS_4)_2$ and (b) $Pd_3(AsSe_4)_2$ monolayers as a function of biaxial strain based on the PBE calculations. Zones I, II, and III correspond to the indirect band gap, direct band gap, and metallic properties, respectively.

potential levels in order to satisfy the conditions for spontaneous water splitting. The water oxidation potential and reduction potential are also dependent on the pH and can be expressed by the following equations:[61,62]

$$E_{O_2/H_2O}{}^{OER} = -5.67 + pH \times 0.059\ eV$$

$$E_{H^+/H_2}{}^{HER} = -4.44 + pH \times 0.059\ eV$$

Therefore, for O_2/H_2O and H^+/H_2 at pH = 0 (pH = 7), respectively, the potential of the standard oxidation and reduction potentials relative to the vacuum level is −5.67 (−5.26) and −4.44 (−4.03) eV. The positions of VBM and CBM of $Pd_3(AsS_4)_2$ and $Pd_3(AsSe_4)_2$ in relation to vacuum level are depicted in Fig. 6b, respectively.

The results demonstrated that $Pd_3(AsSe_4)_2$ monolayer is a promising photocatalyst for OER under visible light irradiation. This is because the VBM is lower than −5.67 eV and the material has good absorption efficiency in the visible light region.

We built a 2 × 2 supercell with 12 Pd, 8 As, and 32 Se atoms for the $Pd_3(AsSe_4)_2$ single-layer. The potential adsorption sites are all thought to be the Pd and Se atoms (Fig. S8†). We discovered that the active site is situated at the Se_2 atom, according to the calculation. The atomic configurations of the intermediates along the water oxidation reaction pathway on the $Pd_3(AsSe_4)_2$ monolayer are shown in Fig. S9,† and the related free-energy profiles under the neutral condition (pH = 7) are summarized in Fig. 7. The black line represents the Gibbs free energy change of the OER for the $Pd_3(AsSe_4)_2$ monolayer when no voltage is applied (U = 0 V), the red line represents the change in Gibbs free energy for the $Pd_3(AsSe_4)_2$ monolayer when exposed to light conditions (U = 1.23 V), and the blue line is the change in Gibbs free energy for the $Pd_3(AsSe_4)_2$ monolayer when the minimum voltage required is applied (U = 1.37 V).

From Fig. 7, we can see that in the third step, the highest Gibbs free energy (∼1.37 eV) is required to oxidize O* species to OOH* species. The photocatalytic oxygen evolution reaction of $Pd_3(AsSe_4)_2$ can proceed smoothly when a voltage of 0.14 V is applied under the light condition of pH = 7. Experimentally, the applied voltages for $Pd_3(AsSe_4)_2$ are feasible, and they are also considerably lower than those for g-C_3N_4 (0.43 V),[27] Ni/graphene composite (0.35 V),[63] C_2N-based type-II heterojunctions (C_2N/GaTe: 1.47 V, C_2N/InTe: 0.94 V),[64] numerous TM@C catalysts

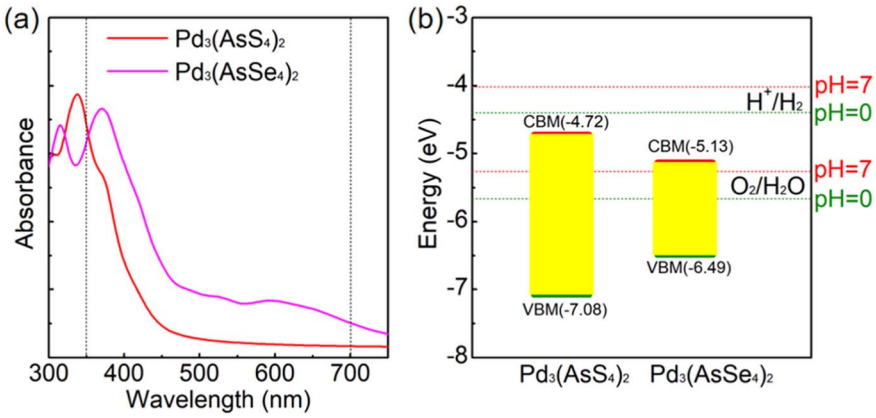

Fig. 6 (a) Light absorption spectra of $Pd_3(AsS_4)_2$ (red line) and $Pd_3(AsSe_4)_2$ monolayers (magenta line) calculated by the HSE06 method. (b) Band edge alignment for water redox reactions of $Pd_3(AsS_4)_2$ (red line) and $Pd_3(AsSe_4)_2$ at pH = 0 and 7.

 © 2023 The Author(s). Published by the Royal Society of Chemistry

Open Access Article. Published on 14 April 2023. Downloaded on 3/13/2026 7:11:50 AM.
This article is licensed under a Creative Commons Attribution-NonCommercial 3.0 Unported Licence.

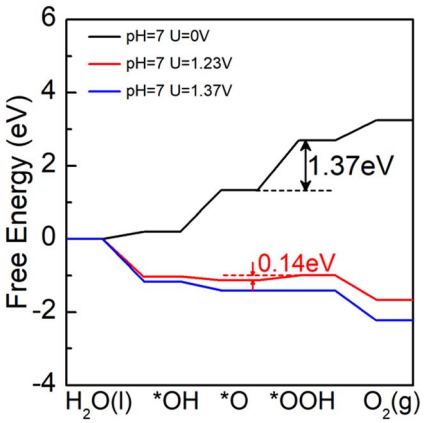

Fig. 7 Gibbs free-energy (ΔG) diagrams for OER on $Pd_3(AsSe_4)_2$ at various electrode potentials.

or metal oxides (0.49–1.7 V),[65] and the extensively researched catalyst γ(Ni, Fe)OOH (0.56 V).[66] It suggests that the $Pd_3(AsSe_4)_2$ has the potential to be an outstanding photocatalyst for water splitting to oxygen evolution.

Conclusions

Motivated by the reports on the synthesis of 2D $Pd_3(PS_4)_2$, an extensive first-principles analysis was carried out to investigate the physical properties of the $Pd_3(AsX_4)_2$ (X = S, Se, Te) monolayers. It is demonstrated that the $Pd_3(AsX_4)_2$ (X = S, Se) monolayers under consideration are dynamical, thermodynamic, chemical, and mechanical stability. By using the HSE06 method, we have shown that $Pd_3(AsX_4)_2$ (X = S and Se) monolayers are electron-transport semiconductors with indirect bandgaps of 2.37 eV and 1.36 eV, respectively. They have high carrier mobility of 523.23 $cm^2\ s^{-1}\ V^{-1}$ and 440.6 $cm^2\ s^{-1}\ V^{-1}$, respectively, which are significantly higher than that of MoS_2 [~200 $cm^2\ s^{-1}\ V^{-1}$]. More specifically, the $Pd_3(AsSe_4)_2$ monolayer exhibits good light absorption in the visible light region. Finally, $Pd_3(AsSe_4)_2$ was proven to be a potential photocatalytic OER catalyst. These findings suggest that the $Pd_3(AsSe_4)_2$ monolayer could be a promising material for the development of efficient photocatalysts for water-splitting applications.

Conflicts of interest

There are no conflicts to declare.

Acknowledgements

This work was supported by the National Natural Science Foundation of China (Grant No. 12164050 and 12264022), Major Science and Technology Project of Precious Metal Materials Genetic Engineering in Yunnan Province (Grant No. 2019ZE001-1, 202002AB080001-6, 2018IC058), Program for Yunling Scholars in Yunnan Province, Program for Donglu Scholars in Yunnan University, Project of the Science Research foundation of the Department of Education in Yunnan Province.

References

1 S. Guo, X. Li, J. Li and B. Wei, *Nat. Commun.*, 2021, **12**, 1343.
2 M. Jeong, I. W. Choi, E. M. Go, Y. Cho, M. Kim, B. Lee, S. Jeong, Y. Jo, H. W. Choi, J. Lee, J.-H. Bae, S. K. Kwak, D. S. Kim and C. Yang, *Science*, 2020, **369**, 1615–1620.
3 K. Maeda and K. Domen, *J. Phys. Chem. Lett.*, 2010, **1**, 2655–2661.
4 X. Li, Z. Li and J. Yang, *Phys. Rev. Lett.*, 2014, **112**, 018301.
5 T. Zhou, Z. Cao, P. Zhang, H. Ma, Z. Gao, H. Wang, Y. Lu, J. He and Y. Zhao, *Sci. Rep.*, 2017, **7**, 46154.
6 M. H. Dahan and M. Caspary Toroker, *J. Phys. Chem. C*, 2017, **121**, 6120–6125.
7 L. Lv, Y. Shen, J. Liu, X. Gao, M. Zhou, Y. Zhang, X. Meng, X. Yang, D. Gong, Y. Zheng and Z. Zhou, *Appl. Surf. Sci.*, 2022, **600**, 154055.
8 A. K. Singh, K. Mathew, H. L. Zhuang and R. G. Hennig, *J. Phys. Chem. Lett.*, 2015, **6**, 1087–1098.
9 Y. Xu, K. Xu, C. Ma, Y. Chen, H. Zhang, Y. Liu and Y. Ji, *J. Mater. Chem. A*, 2020, **8**, 19612–19622.
10 Y. Zhang, Y. Shen, J. Liu, L. Lv, X. Gao, M. Zhou, X. Yang, X. Meng, Y. Zheng and Z. Zhou, *Appl. Surf. Sci.*, 2022, **604**, 154555.
11 X. Yang, Y. Shen, J. Liu, X. Meng, X. Gao, L. Lv, M. Zhou, Y. Zhang, Y. Zheng and Z. Zhou, *Phys. Chem. Chem. Phys.*, 2022, **24**, 7642–7652.
12 A. Fujishima and K. Honda, *Nature*, 1972, **238**, 37–38.
13 S. Lin, H. Huang, T. Ma and Y. Zhang, *Adv. Sci.*, 2021, **8**, 2002458.
14 A. S. Malik, T. Liu, M. Rittiruam, T. Saelee, J. L. F. Da Silva, S. Praserthdam and P. Praserthdam, *Sci. Rep.*, 2022, **12**, 2604.
15 K. S. Novoselov, A. K. Geim, S. V. Morozov, D. Jiang, Y. Zhang, S. V. Dubonos, I. V. Grigorieva and A. A. Firsov, *Science*, 2004, **306**, 666–669.
16 J. Qiao, X. Kong, Z.-X. Hu, F. Yang and W. Ji, *Nat. Commun.*, 2014, **5**, 4475.
17 D. Sarkar, W. Liu, X. Xie, A. C. Anselmo, S. Mitragotri and K. Banerjee, *ACS Nano*, 2014, **8**, 3992–4003.
18 F. Xia, D. B. Farmer, Y.-m. Lin and P. Avouris, *Nano Lett.*, 2010, **10**, 715–718.
19 H. Liu, A. T. Neal, Z. Zhu, Z. Luo, X. Xu, D. Tománek and P. D. Ye, *ACS Nano*, 2014, **8**, 4033–4041.
20 A. Bandyopadhyay, D. Ghosh and S. K. Pati, *J. Phys. Chem. Lett.*, 2018, **9**, 1605–1612.
21 F. Xia, H. Wang, D. Xiao, M. Dubey and A. Ramasubramaniam, *Nat. Photonics*, 2014, **8**, 899–907.
22 Z. Sun, A. Martinez and F. Wang, *Nat. Photonics*, 2016, **10**, 227–238.
23 F. H. L. Koppens, T. Mueller, P. Avouris, A. C. Ferrari, M. S. Vitiello and M. Polini, *Nat. Nanotechnol.*, 2014, **9**, 780–793.
24 A. N. Grigorenko, M. Polini and K. S. Novoselov, *Nat. Photonics*, 2012, **6**, 749–758.

Open Access Article. Published on 14 April 2023. Downloaded on 3/13/2026 7:11:50 AM.
This article is licensed under a Creative Commons Attribution-NonCommercial 3.0 Unported Licence.

25 F. H. L. Koppens, D. E. Chang and F. J. García de Abajo, *Nano Lett.*, 2011, **11**, 3370–3377.
26 A. Agarwal, M. S. Vitiello, L. Viti, A. Cupolillo and A. Politano, *Nanoscale*, 2018, **10**, 8938–8946.
27 J. Wirth, R. Neumann, M. Antonietti and P. Saalfrank, *Phys. Chem. Chem. Phys.*, 2014, **16**, 15917–15926.
28 T. A. Bither, P. C. Donohue and H. S. Young, *J. Solid State Chem.*, 1971, **3**, 300–307.
29 Y. Jing and T. Heine, *J. Mater. Chem. A*, 2018, **6**, 23495–23501.
30 C. Tang, C. Zhang, S. K. Matta, Y. Jiao, K. Ostrikov, T. Liao, L. Kou and A. Du, *J. Phys. Chem. C*, 2018, **122**, 21927–21932.
31 Y. Shan, T. Li and L. Liu, *Solid State Commun.*, 2020, **306**, 113786.
32 S. Yan, B.-C. Gong, L. Wang, J. Wu, Q. Yin, X. Cao, X. Zhang, X. Liu, Z.-Y. Lu, K. Liu and H. Lei, *Phys. Rev. B*, 2022, **105**, 155115.
33 G. Kresse and J. Furthmüller, *Phys. Rev. B: Condens. Matter Mater. Phys.*, 1996, **54**, 11169–11186.
34 P. E. Blöchl, *Phys. Rev. B: Condens. Matter Mater. Phys.*, 1994, **50**, 17953–17979.
35 J. P. Perdew, K. Burke and M. Ernzerhof, *Phys. Rev. Lett.*, 1996, **77**, 3865–3868.
36 J. Heyd, G. E. Scuseria and M. Ernzerhof, *J. Chem. Phys.*, 2003, **118**, 8207–8215.
37 A. Togo, F. Oba and I. Tanaka, *Phys. Rev. B: Condens. Matter Mater. Phys.*, 2008, **78**, 134106.
38 S. Baroni, S. de Gironcoli, A. Dal Corso and P. Giannozzi, *Rev. Mod. Phys.*, 2001, **73**, 515–562.
39 X. Huang, T. R. Paudel, S. Dong and E. Y. Tsymbal, *Phys. Rev. B: Condens. Matter Mater. Phys.*, 2015, **92**, 125201.
40 M. Shahrokhi and C. Leonard, *J. Alloys Compd.*, 2016, **682**, 254–262.
41 H. Li, J. Wang, R. Qi, Y. Hu, J. Zhang, H. Zhao, J. Zhang and Y. Zhao, *Appl. Catal., B*, 2021, **285**, 119778.
42 J. K. Nørskov, J. Rossmeisl, A. Logadottir, L. Lindqvist, J. R. Kitchin, T. Bligaard and H. Jónsson, *J. Phys. Chem. B*, 2004, **108**, 17886–17892.
43 L. Lv, Z. Li, K.-H. Xue, Y. Ruan, X. Ao, H. Wan, X. Miao, B. Zhang, J. Jiang, C. Wang and K. Ostrikov, *Nano Energy*, 2018, **47**, 275–284.
44 L.-M. Yang, V. Bačić, I. A. Popov, A. I. Boldyrev, T. Heine, T. Frauenheim and E. Ganz, *J. Am. Chem. Soc.*, 2015, **137**, 2757–2762.
45 A. A. Emery and C. Wolverton, *Sci. Data*, 2017, **4**, 170153.
46 K. Kuhar, A. Crovetto, M. Pandey, K. S. Thygesen, B. Seger, P. C. K. Vesborg, O. Hansen, I. Chorkendorff and K. W. Jacobsen, *Energy Environ. Sci.*, 2017, **10**, 2579–2593.
47 Z.-j. Wu, E.-j. Zhao, H.-p. Xiang, X.-f. Hao, X.-j. Liu and J. Meng, *Phys. Rev. B: Condens. Matter Mater. Phys.*, 2007, **76**, 054115.
48 Y. Gao, Z. Wang and L. Chen, *J. Mater. Chem. A*, 2015, **3**, 23420–23425.
49 Y. Cai, G. Zhang and Y.-W. Zhang, *Sci. Rep.*, 2014, **4**, 6677.
50 H. Xiao, J. Tahir-Kheli and W. A. Goddard III, *J. Phys. Chem. Lett.*, 2011, **2**, 212–217.
51 M. Ni, M. K. H. Leung, D. Y. C. Leung and K. Sumathy, *Renewable Sustainable Energy Rev.*, 2007, **11**, 401–425.
52 M. Jakhar, A. Kumar, P. K. Ahluwalia, K. Tankeshwar and R. Pandey, *Materials*, 2022, **15**, 2221.
53 J. Bardeen and W. Shockley, *Phys. Rev.*, 1950, **80**, 72–80.
54 K. Kaasbjerg, K. S. Thygesen and K. W. Jacobsen, *Phys. Rev. B: Condens. Matter Mater. Phys.*, 2012, **85**, 115317.
55 Q. H. Wang, K. Kalantar-Zadeh, A. Kis, J. N. Coleman and M. S. Strano, *Nat. Nanotechnol.*, 2012, **7**, 699–712.
56 H. Zhang, Z. Fu, R. Zhang, Q. Zhang, H. Tian, D. Legut, T. C. Germann, Y. Guo, S. Du and J. S. Francisco, *Proc. Natl. Acad. Sci.*, 2017, **114**, E11082–E11091.
57 Z. Fu, H. Zhang, C. Si, D. Legut, T. C. Germann, Q. Zhang, S. Du, J. S. Francisco and R. Zhang, *J. Phys. Chem. C*, 2018, **122**, 4710–4722.
58 T. Li, *Phys. Rev. B: Condens. Matter Mater. Phys.*, 2012, **85**, 235407.
59 B. Mortazavi and G. Cuniberti, *Nanotechnology*, 2014, **25**, 215704.
60 S. K. Matta, C. Zhang, Y. Jiao, A. O'Mullane and A. Du, *Nanoscale*, 2018, **10**, 6369–6374.
61 J. Li, Z. Huang, W. Ke, J. Yu, K. Ren and Z. Dong, *J. Alloys Compd.*, 2021, **866**, 158774.
62 M. Naseri, A. Bafekry, M. Faraji, D. M. Hoat, M. M. Fadlallah, M. Ghergherehchi, N. Sabbaghi and D. Gogova, *Phys. Chem. Chem. Phys.*, 2021, **23**, 12226–12232.
63 G. Gao, S. Bottle and A. Du, *Catal. Sci. Technol.*, 2018, **8**, 996–1001.
64 X. Zhang, A. Chen, Z. Zhang, M. Jiao and Z. Zhou, *Nanoscale Adv.*, 2019, **1**, 154–161.
65 X. Cui, P. Ren, D. Deng, J. Deng and X. Bao, *Energy Environ. Sci.*, 2016, **9**, 123–129.
66 D. Friebel, M. W. Louie, M. Bajdich, K. E. Sanwald, Y. Cai, A. M. Wise, M.-J. Cheng, D. Sokaras, T.-C. Weng, R. Alonso-Mori, R. C. Davis, J. R. Bargar, J. K. Nørskov, A. Nilsson and A. T. Bell, *J. Am. Chem. Soc.*, 2015, **137**, 1305–1313.

 © 2023 The Author(s). Published by the Royal Society of Chemistry